Electronic Supplementary Information (ESI) for

All-inorganic copper-halide perovskites for large-stokes-shift and ten-nanosecond-emission scintillators

Tobias Haposan,[a] Arramel Arramel,[*b] Pramitha Yuniar Diah Maulida,[b] Sri Hartati,[b] Afif Akmal Afkauni,[b] Muhammad Haris Mahyuddin,[c,d] Lei Zhang,[e] Dominik Kowal,[f] Marcin Eugeniusz Witkowski,[g] Konrad Jacek Drozdowski,[g] Michal Makowski,[f] Winicjusz Drozdowski,[g] Lina Jaya Diguna,[*a] and Muhammad Danang Birowosuto,[*f]

---

[a] Department of Renewable Energy Engineering, Universitas Prasetiya Mulya, Kavling Edutown I.1, Jl. BSD Raya Utama, Tangerang 15339, Indonesia. E-mail: lina.diguna@prasetiyamulya.ac.id

[b] Nano Center Indonesia, Jl. PUSPIPTEK, Tangerang Selatan 15314, Indonesia. E-mail: arramel@nano.or.id

[c] Quantum and Nano Technology Research Group, Institut Teknologi Bandung, Jl. Ganesha 10, Bandung 40132, Indonesia.

[d] Research Center for Nanoscience and Nanotechnology, Institut Teknologi Bandung, Jl. Ganesha 10, Bandung 40132, Indonesia.

[e] Department of Physics, National University of Singapore, 2 Science Drive 3, Singapore 117542, Singapore.

[f] Łukasiewicz Research Network-PORT Polish Center for Technology Development, Stabłowicka 147, 54-066 Wrocław, Poland. E-mail: muhammad.birowosuto@port.lukasiewicz.gov.pl

[g] Institute of Physics, Faculty of Physics, Astronomy, and Informatics, Nicolaus Copernicus University in Torun, ul. Grudziadzka 5, 87-100 Torun, Poland.

List of Figures

List of Tables

After-grinding powder under 254 nm light

Figure S1: The photograph of (a) $CsCu_2I_3$, (b) $Cs_3Cu_2I_5$, (c) $Cs_3Cu_2I_4Br$, and (d) $Cs_3Cu_2I_3Br_2$ under 254 nm light.

SEM and TEM
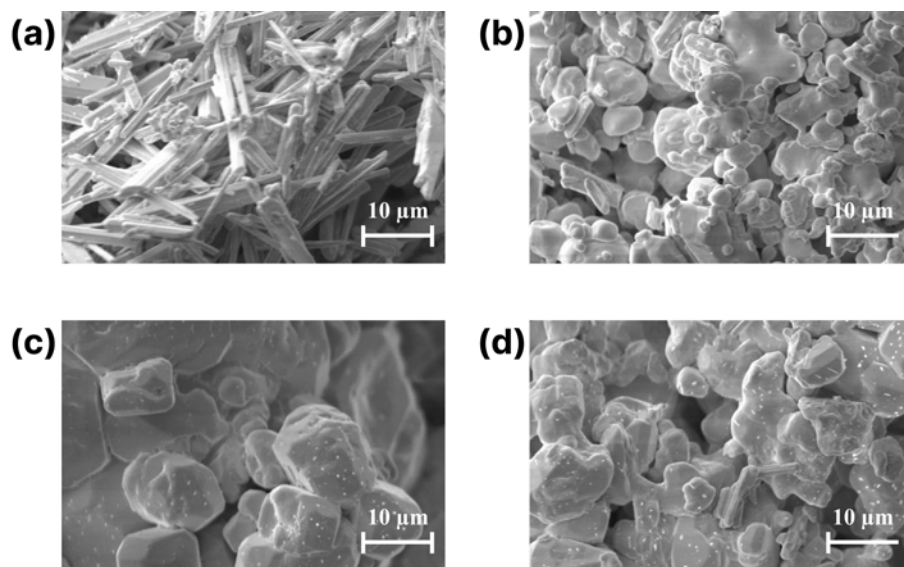
Figure S2: SEM images of (a) $CsCu_2I_3$, (b) $Cs_3Cu_2I_5$, (c) $Cs_3Cu_2I_4Br$, and (d) $Cs_3Cu_2I_3Br_2$ powder.
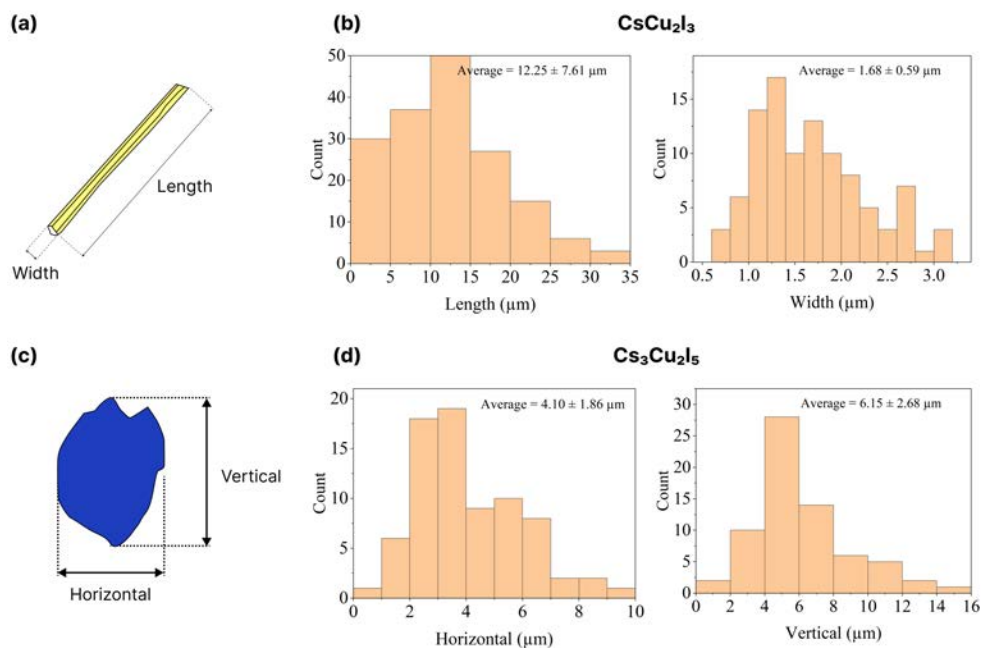
Figure S3: Distribution of dimensions of the CHP clusters from the SEM images. (a) Illustration of $CsCu_2I_3$ with the length and width dimensions and its (b) distribution histograms of length (left) and width (right) dimensions. (c) Illustration of $Cs_3Cu_2I_5$ with the horizontal and vertical diameters and its (d) distribution histograms of horizontal (left) and vertical (right) diameters. For $CsCu_2I_3$, it is apparent that the rod-like shape is common with approximately 7:1 ratio between length and width average.

To unveil the morphological state at greater magnifications of the $CsCu_2I_3$ and $Cs_3Cu_2I_5$, we carried out transmission electron microscopy (TEM) and high-resolution TEM (HRTEM) as depicted in Figure S4. As explained in the Experimental section, the samples were prepared by sonification in a dispersed solution, hence separating the aggregated clustered powder form into individual nanocrystals. TEM and HRTEM of $CsCu_2I_3$ are depicted in Figure S4a, with the size
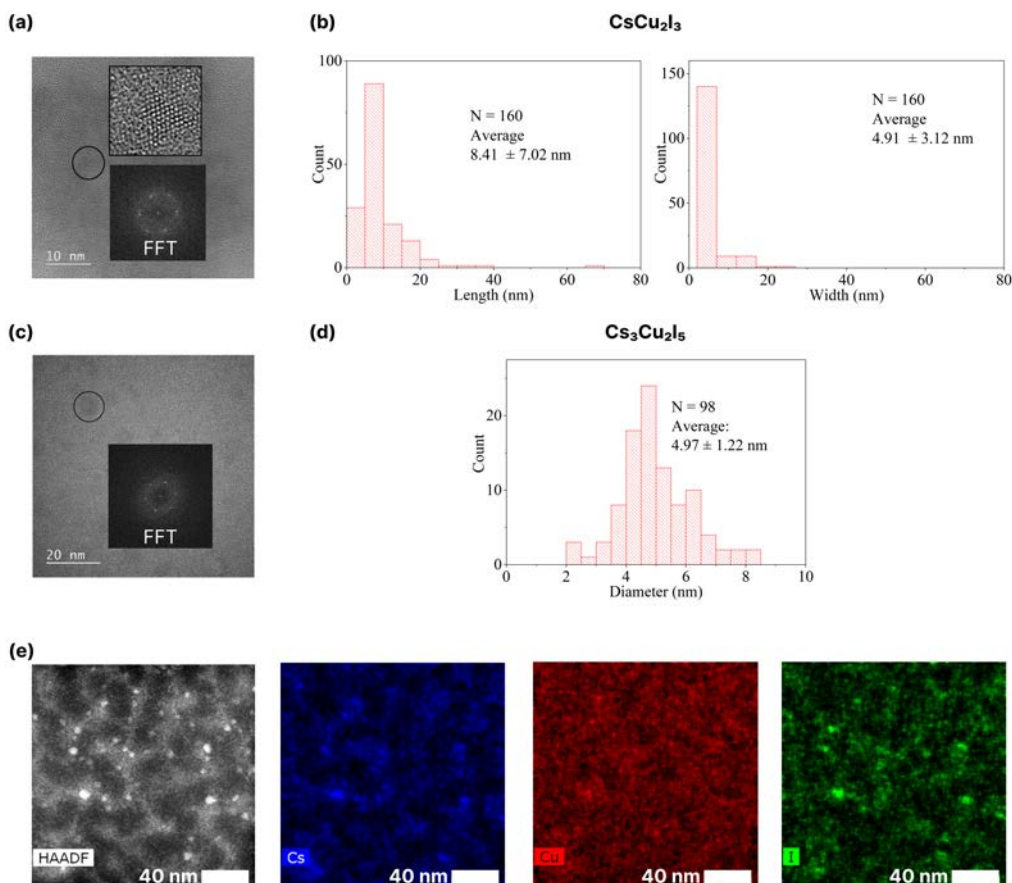
Figure S4: (a) TEM, HRTEM, and fast-Fourier transform (FFT) image of $CsCu_2I_3$ nanocrystals after sonification and filtering with their (b) dimension distribution in length (left) and width (right). (c) TEM, HRTEM, and FFT image of $Cs_3Cu_2I_5$ nanocrystals with their (d) particle size distribution. (e) Energy dispersive X-ray spectroscopy (EDS) elemental mapping of Cs, Cu, and I in $Cs_3Cu_2I_5$.

distribution in Figure S4b indicating the consistent rod-like shape as found in SEM. Similarly, the TEM of $Cs_3Cu_2I_5$ with its particle size distribution are depicted in Figures S4c and S4d, respectively. Furthermore, the distorted hexagons obtained from the of HRTEM indicate the formation of an orthorhombic structure. This finding provides insight into producing CHP nanocrystals through mechanochemistry, as an alternative to the hot-injection method.

Rietveld refinement
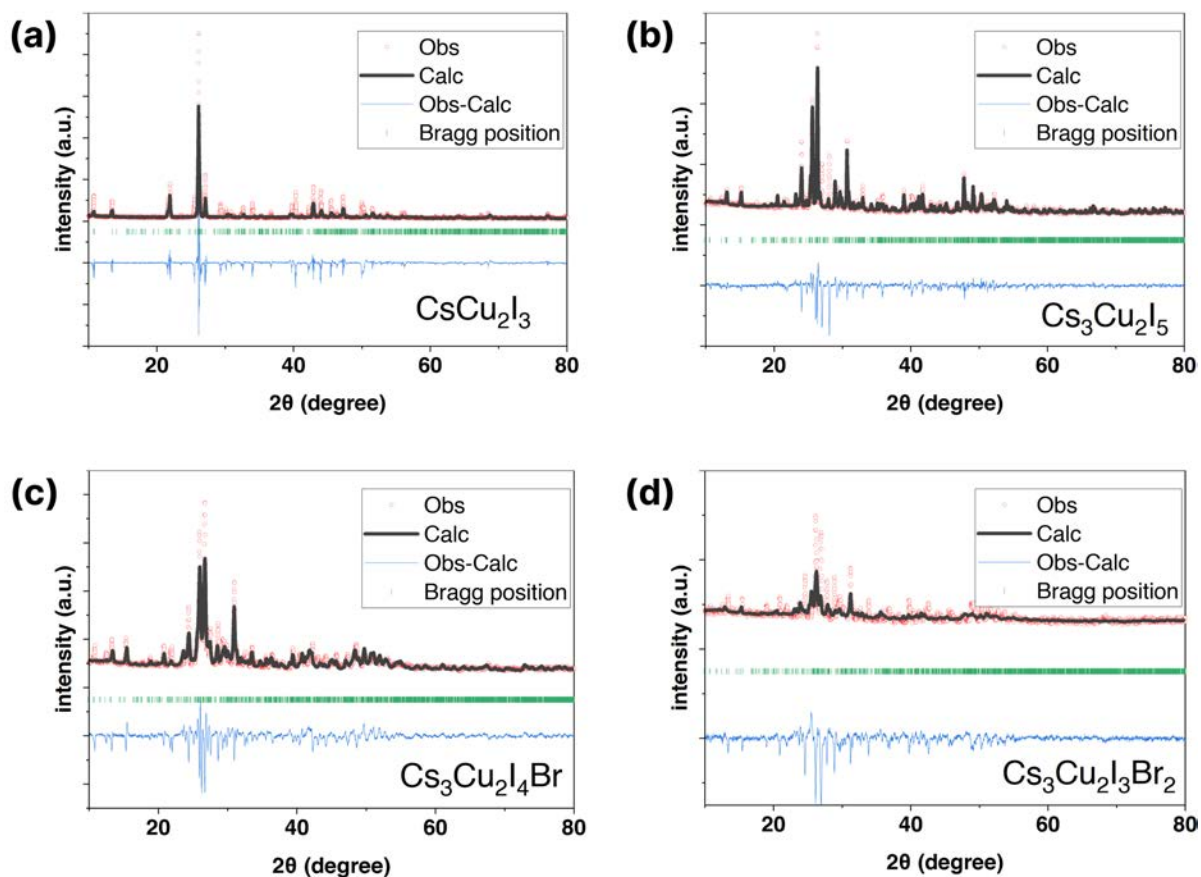
Figure S5: Experimental (black circles), Rietveld refinement (black line), its difference (blue line), and Bragg positions of XRD pattern from (a) $CsCu_2I_3$, (b) $Cs_3Cu_2I_5$, (c) $Cs_3Cu_2I_4Br$, and (d) $Cs_3Cu_2I_3Br_2$, carried out inside Profex software package.[1] We note that the calculated CIFs for $CsCu_2I_3$ and $Cs_3Cu_2I_5$ were adapted from reference,[2] whereas for the case of $Cs_3Cu_2I_4Br$ and $Cs_3Cu_2I_3Br_2$ were determined based on the theoretical procedure outlined in the Experimental section.

Table S1: Lattice parameters of the copper halide perovskites (CHPs) obtained by Rietveld refinement of experimental XRD patterns at room temperature.

Compounds	*Space group*	*a* (Å)	*b* (Å)	*c* (Å)	*V* (Å³)	R_{wp} (%)	χ^2
$CsCu_2I_3$	*Cmcm*	10.439 ± 0.001	13.154 ± 0.0002	6.284 ± 0.00007	865.204 ± 0.841	26.12	15.29
$Cs_3Cu_2I_5$	*Pnma*	10.289 ± 0.001	11.669 ± 0.00008	14.428 ± 0.001	1698.750 ± 0.046	12.16	9.51
$Cs_3Cu_2I_4Br$	*Pnma*	10.125 ± 0.001	11.648 ± 0.0002	14.399 ± 0.001	1679.527 ± 0.047	13.11	17.54
$Cs_3Cu_2I_3Br_2$	*Pnma*	10.154 ± 0.0006	11.368 ± 0.001	14.257 ± 0.001	1637.956 ± 0.617	12.45	12.37

Fourier-transformed infrared spectroscopy
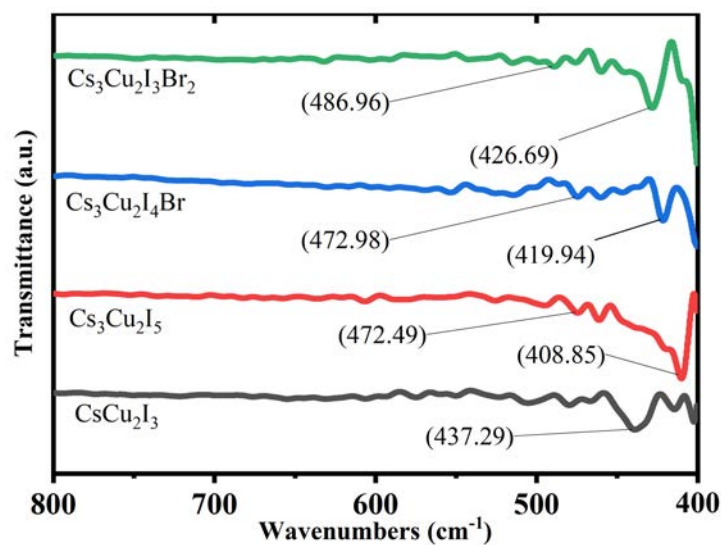
Figure S6: FTIR spectra of the CHPs measured at room temperature.

Fingerprint FTIR spectra, as shown in Figure S6, show that the addition of Br results in a blue shift, as a dip at wavenumber $\sim$408.85 cm^{-1} in $Cs_3Cu_2I_5$ shifts to $\sim$419.94 cm^{-1} and $\sim$426.69 cm^{-1} in $Cs_3Cu_2I_4Br$ and $Cs_3Cu_2I_3Br_2$ respectively. A similar blue shift is also shown by a dip at wavenumber $\sim$472.49 cm^{-1} in $Cs_3Cu_2I_5$ shifts to $\sim$472.98 cm^{-1} and $\sim$486.96 cm^{-1} in $Cs_3Cu_2I_4Br$ and $Cs_3Cu_2I_3Br_2$ respectively. A similar trend is also suggested by changing the dimensionality from 0D to 1D. The observed spectral bands may be attributed to the infrared-active stretching vibrations of metal-halogen bonds in inorganic complexes, positioned within the wavenumber range of 500-200 cm^{-1}.[7]

Raman spectra
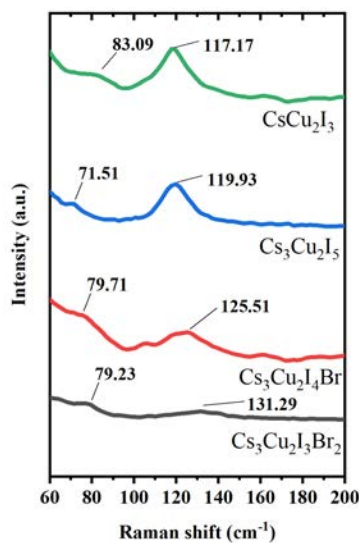
Figure S7: Raman spectra of the CHPs at room temperature.

Figure S7 shows Raman spectra of the CHPs. The main peak observed at ∼120 cm^{-1} for all samples is attributed to I-Cu-I vibration mode.[8] ~~and~~ It tends to shift to higher wavenumber, as well as the dimensionality is reduced from 1D structure in $CsCu_2I_3$ to 0D structure in $Cs_3Cu_2I_5$ and when the I is substituted with Br. We suspect that the observed phenomena may be caused by the phonon confinement effect.[9] The shifting to a higher wavenumber as the ~~increasing~~ increase of Br species is due to a minute change of lattice-phonon coupling in the inorganic networks. This interaction is ~~cause~~ caused by the lowering of unit cell dimensions when incorporating the smaller Br atoms in the lattice and in turn causes stiffening of the lattice, thus a shift to higher frequency occurs.[10,11] Furthermore, the signal (weak protrusion) at ∼80 cm^{-1} can be tentatively corresponded to the two-phonon difference between the longitudinal-optic and transverse-optic modes.[12]

X-ray photoelectron spectroscopy
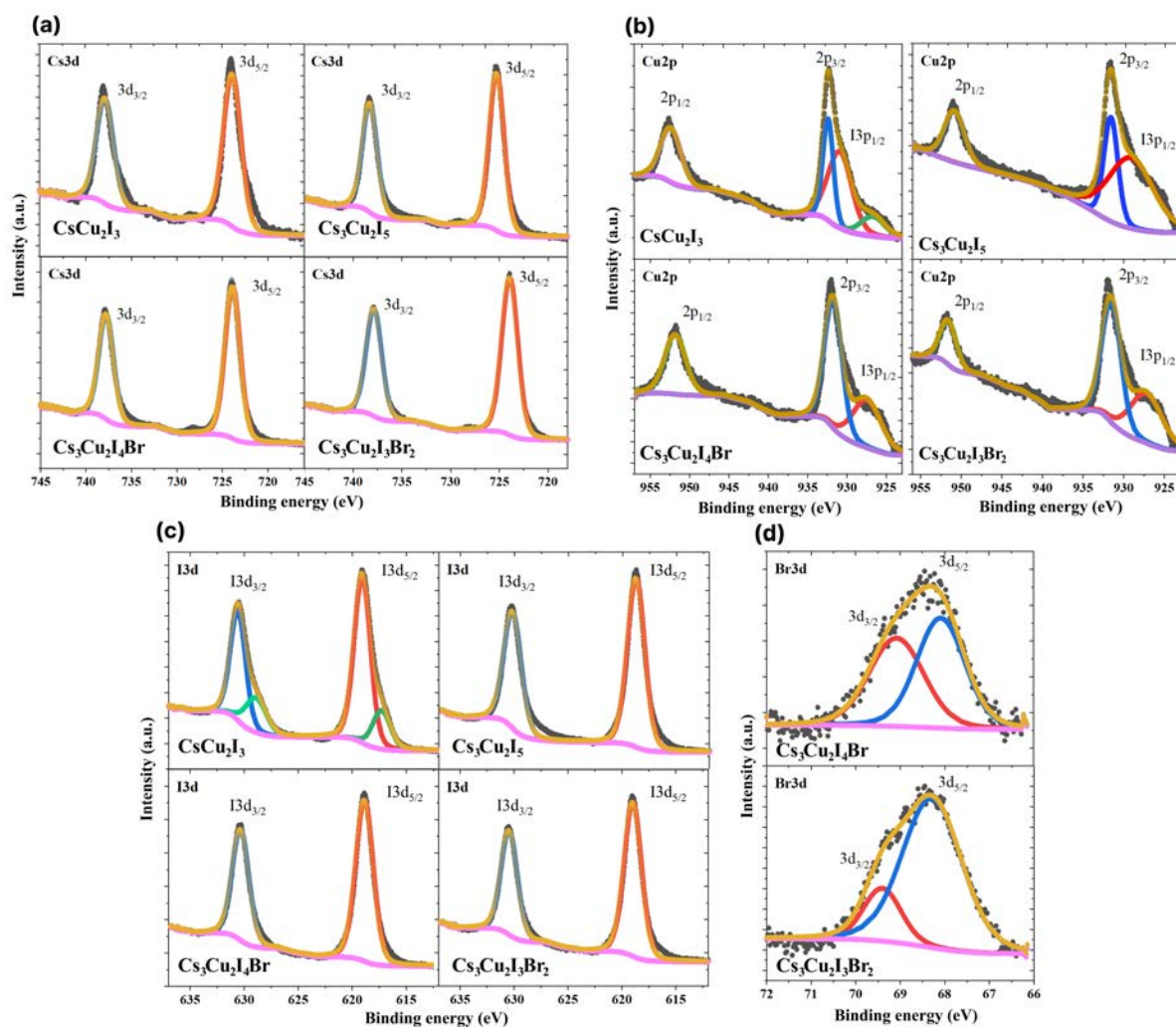
Figure S8: Deconvoluted XPS spectra of the CHPs on the region of (a) Cs3d, (b) Cu2p, (c) I3d, and (d) Br3d.

We performed a series of high-resolution XPS measurements on the CHPs to determine the surface composition of the CHPs depicted in Figure S8a-d. In all Cs 3d peaks (Figure S8a), two symmetrical peaks are observed located at the binding energy of ∼738 and ∼724 eV for Cs orbital $3d_{3/2}$ and $3d_{5/2}$, respectively for all CHPs.[13] The core level spectra of Cu2p in 1D $CsCu_2I_3$ and 0D $Cs_3Cu_2I_5$ CHPs (Figure S8b) share similar two major peaks located at ∼951 and ∼932 eV, which can be assigned to the Cu $2p_{1/2}$ and Cu $2p_{3/2}$, respectively.[14] The absence of satellite peak at 934 eV suggests that the Cu adopts a monovalent Cu^+ configuration.[15,16] The fitted XPS spectra of $Cu2p_{3/2}$ region in 1D $Cs_3Cu_2I_5$ consisted of three deconvoluted peaks. The blue line is centered at 932 eV corresponds to the Cu $2p_{3/2}$ in a +1 oxidation state,[15] whereas the black line located at 931 eV corresponds to I $3p_{1/2}$,[17,18] and the small shoulder peak in green located in 927 eV corresponds to Cs MNN electron.[19] Interestingly, the fitted high resolution XPS spectra for the other three samples show Cu $2p_{3/2}$ comprised of only two peaks. On all CHPs, the distance between two peaks on the Cu 2p survey region remains consistent at ∼20 eV. Survey of I 3d orbital (Figure S8c) shows a symmetric peak located at ∼630 and ∼619 eV for $I3d_{3/2}$ and I $3d_{5/2}$, respectively for $Cs_3Cu_2I_5$, $Cs_3Cu_2I_4Br$, and $Cs_3Cu_2I_3Br_2$.[18] Meanwhile the fitted XPS spectra for $CsCu_2I_3$ shows different peak compositions than the other three CHPs. For 1D $CsCu_2I_3$, in addition to the usual peaks of I $3d_{3/2}$ and $I3d_{5/2}$, another small

shoulder peaks were found in the lower binding energy of the main peak located at ~629 and ~617 eV may be attributed to different I chemical environment such as Cs—I for each of the I 3d XPS peak.[13] In $Cs_3Cu_2I_4Br$ and $Cs_3Cu_2I_3Br_2$, peaks appear at ~69 and ~68 eV, confirming the presence of Br in the respective CHPs.

Table S2: A summary of the XPS deconvoluted spectra FWHM and area evaluation. For XPS analyses, the CasaXPS software package was used.[6]

CHP	Orbital	FWHM (eV)	Area
$CsCu_2I_3$	Cs3d	2.41	63394.09
	Cu2p	3.24	105461.60
	I3d	2.49	151412.07
$Cs_3Cu_2I_5$	Cs3d	2.21	93238.77
	Cu2p	4.20	122942.10
	I3d	2.31	116023.58
$Cs_3Cu_2I_4Br$	Cs3d	2.45	61005.14
	Cu2p	4.49	57959.72
	I3d	2.46	57357.07
	Br3d	3.60	2914.25
$Cs_3Cu_2I_3Br_2$	Cs3d	2.30	99229.70
	Cu2p	3.81	88263.33
	I3d	2.28	77197.88
	Br3d	3.73	15232.57

Absorption spectra

Experimental band gap was obtained with Elliot fitting.[3] In principle, the contributions to the absorption coefficient (α) can be defined from free carriers (continuum) (α_c) and excitons (α_{ex}), as shown in Eq. S1. α_{ex} can be obtained with Eq. S2, where the frequency dependence of P_{cv} is approximated as a constant and related to the interband transition matrix element, $\hbar\omega$ is the photon energy, $\theta(\hbar\omega - E_g)$ is the Heaviside step function, x is defined as $\sqrt{R_{ex}/(\hbar\omega - E_g)}$, and δ denotes a delta function. R_{ex} is exciton Rydberg energy; n is the principle quantum number. The fits are shown in Figure S9.

$$\alpha(\hbar\omega) = \alpha_c + \alpha_{ex} \tag{S1}$$

$$\alpha(\hbar\omega) = P_{cv}\left[\theta(\hbar\omega - E_g) \cdot \left(\frac{\pi e^{\pi x}}{sinh(\pi x)}\right) + R_{ex}\sum_{n=1}^{\infty}\frac{4\pi}{n^3} \cdot \delta(\hbar\omega - E_g + \frac{R_{ex}}{n^2})\right] \tag{S2}$$
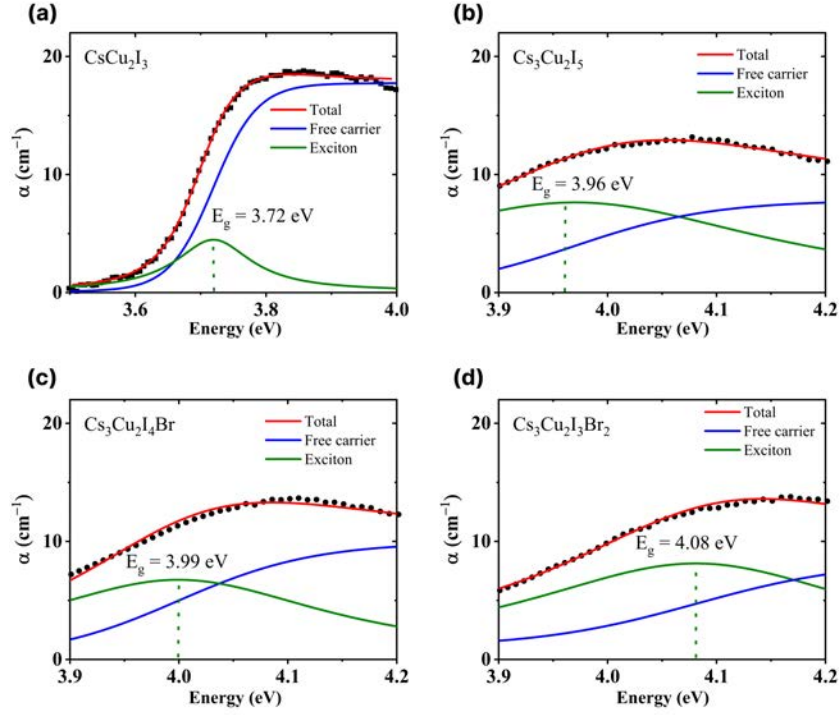
Figure S9: Absorption spectra and their fitting curves of (a) $CsCu_2I_3$, (b) $Cs_3Cu_2I_5$, (c) $Cs_3Cu_2I_4Br$, and (d) $Cs_3Cu_2I_3Br_2$, determined with the Elliot fit[3] method as explained in Eqs. S1 and S2.
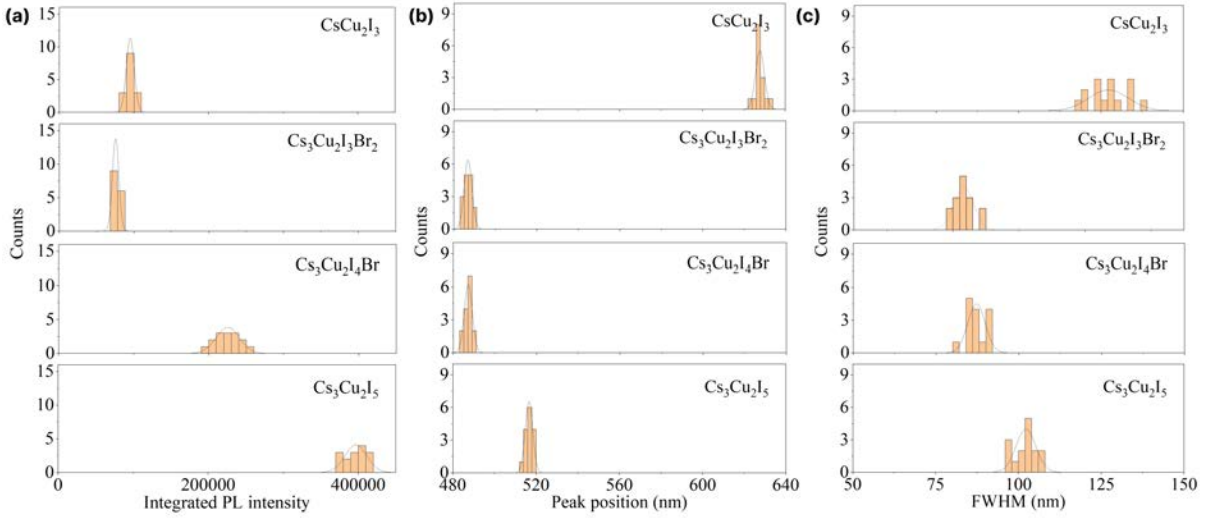
Figure S10: Distribution of PL results, namely (a) integrated PL intensity, (b) PL peak positions, and (c) FWHM of the CHPs from multiple series of and experiments.

13

Summary of optical properties of Pb-based perovskites

Table S3: Summary of optical properties of representative perovskites (all measured at RT)

Perovskite	Absorption peak (nm)	PL peak (nm)	FWHM (nm)	Stokes shift (nm)	Ref.
$CsPbI_3$ nanocrystals	664	667	36	3	[20]
$CsPbBr_3$ nanocrystals	480	517	33	37	[20]
Cs_4PbI_6 single crystal	341	547	200	206	[21]
Dual-phase $Cs_4PbBr_6/CsPbBr_3$	510	518	30	8	[22]
Dual-phase $CsPbBr_3$-$CsPb_2Br_5$	346	522	21.2	176	[23]
$CsPbBr_3$ nanosheets	460	515	21	55	[24]
$CsPbBr_3$ nanowires in anodised aluminum oxide	$\sim$530	530	30	$\sim$0	[25]
$CsCu_2I_3$	323.27	628.87 ± 3.18	127.31 ± 6.05	294.49 ± 2.81	This work
$Cs_3Cu_2I_5$	303.08	518.54 ± 2.73	102.26 ± 3.01	203.54 ± 4.35	
$Cs_3Cu_2I_4Br$	301.74	487.36 ± 2.45	87.18 ± 2.66	119.31 ± 21.92	
$Cs_3Cu_2I_3Br_2$	298.38	485.25 ± 2.43	83.26 ± 3.00	176.08 ± 3.00	

Glow curve fitting

For the quantitative analysis, we deconvolute the glow curves into k glow peaks, based on the classic Randall-Wilkins equation:[4,5]

$$I_{TL} = \sum_{i=1}^{k} n_{0_i} V \sigma_i \exp\left(-\frac{E_i}{k_B T}\right) \exp\left(-\frac{\sigma_i}{\beta} \int_{T_0}^{T} \exp\left(-\frac{E_i}{k_B T'}\right) dT'\right) \tag{S3}$$

where T is the temperature, β is the heating rate, k_B is the Boltzmann constant, n_{0_i} is the initial trap concentration, V is the crystal volume, E_i is the trap depth, and σ_i is the frequency factor of each component. The unit-less $n_{0_i} V$ or A_i, shown in Figure S11, is used to compare afterglow of different crystals.
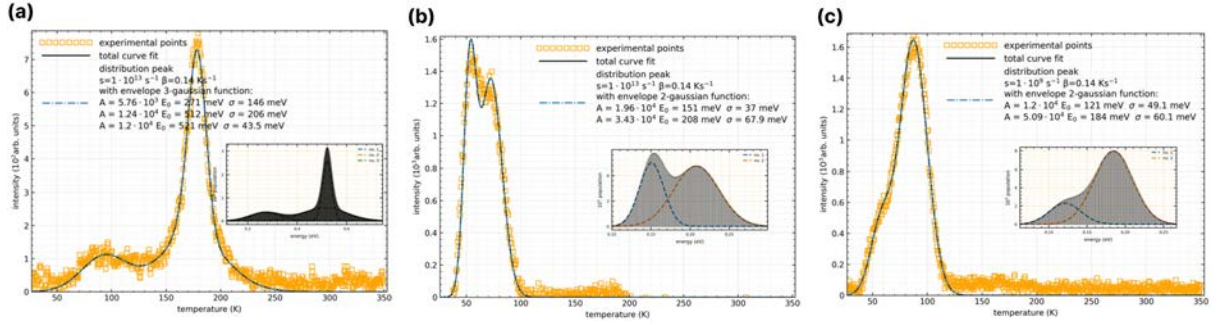
Figure S11: Glow curve fitting of (a) $Cs_3Cu_2I_5$, (b) $Cs_3Cu_2I_4Br$, and (c) $Cs_3Cu_2I_3Br_2$ with multiple Randal-Wilkins equation.[4,5] The parameters used for fitting are shown in the inset.

Table S4: Parameter of the TL peak fitting, where T_{max} is the temperature at which the maximum of peak occurs, E is the depth of trap, n_0 is the trap concentration, and σ is frequency factor.

CHP	T_{max} (K)	E (meV)	n_0 (a.u.)	σ (meV)
$CsCu_2I_3$			No trap	
	95	271 ± 27	$(5.76 \pm 0.58) \times 10^3$	146 ± 15
$Cs_3Cu_2I_5$	162	512 ± 26	$(1.24 \pm 0.06) \times 10^4$	206 ± 10
	175	521 ± 26	$(1.20 \pm 0.06) \times 10^4$	43.5 ± 2
$Cs_3Cu_2I_4Br$	54	151 ± 15	$(1.96 \pm 0.20) \times 10^4$	37 ± 7
	72	208 ± 21	$(3.43 \pm 0.34) \times 10^4$	67.9 ± 7
$Cs_3Cu_2I_3Br_2$	61	121 ± 18	$(1.20 \pm 0.20) \times 10^4$	49.1 ± 7
	84	184 ± 18	$(5.09 \pm 0.34) \times 10^4$	60.1 ± 6

Quantum yield
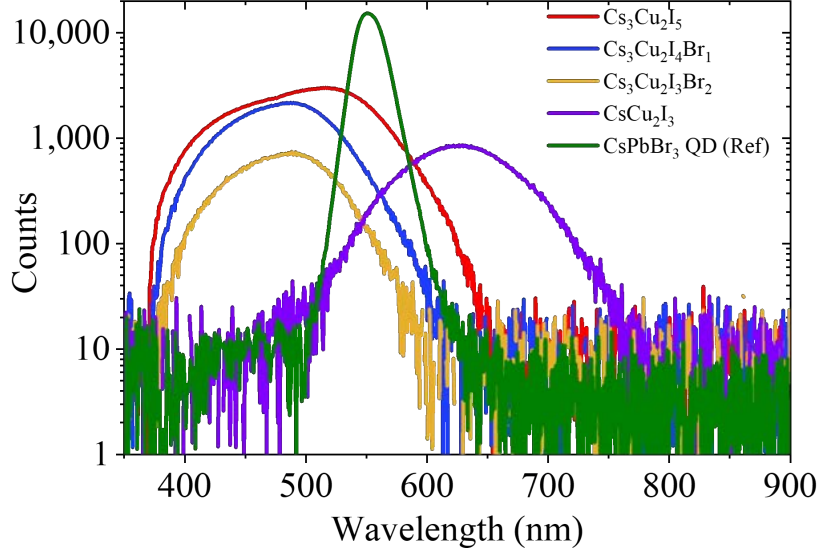
Figure S12: Fluorescence spectra of $Cs_3Cu_2I_5$ (black), $Cs_3Cu_2I_4Br$ (blue), $Cs_3Cu_2I_3Br_2$ (yellow), $CsCu_2I_3$ (purple), and $CsPbBr_3$ quantum dots (QDs) (dark green).

For reference purposes, we employed $CsPbBr_3$ quantum dots (QDs) integrated into the resin without requiring additional purification, as outlined in previous work.[26] Notably, information from a private communication[27] indicates Q_r to be 64%, nr as 2.3, and Ar as 0.85. In order to calculate the QY of the sample (Q_s):

$$Q_s = Q_r \left(\frac{A_r}{A} \right) \left(\frac{E_s}{E_r} \right) \left(\frac{n_s}{n_r} \right)^2 \tag{S4}$$

where Q is the fluorescence quantum yield, n is the refractive index of the QDs/crystals, A is the absorbance of the QDs/crystals, and E is the integrated fluorescence intensity of the emitted light. The subscript "s" and "r" refer to the reference and unknown fluorophore, respectively. The experimental results can be found in Figure S12.

Through the conducted analyses, the QY (expressed in %) have been ascertained as displayed in Table 3 in the manuscript. The QY of $Cs_3Cu_2I_5$, accounting for 47%, aligns with the 51% reported in Zhao *et al.*[28] Meanwhile, the reduced QY of $CsCu_2I_3$ resembles that found in reference.[19] The observed trend of decreasing QY with increasing bromide concentration in the mixed bromide and iodide samples can be anticipated due to the reduction in refractive index.[29]

16

Pulse-height spectra
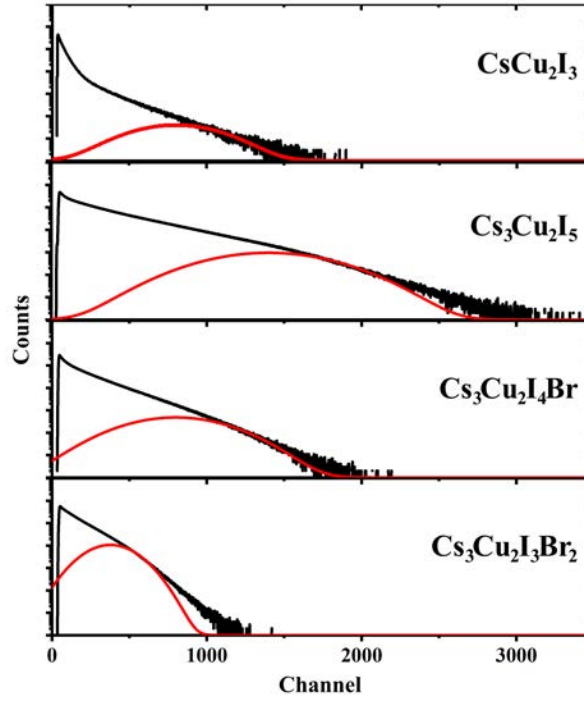
Figure S13: Pulse height spectra of the CHPs, using a ^{137}Cs source.

Herein, an additional pulse height spectra measured with 661.7 keV gamma-ray source as shown in Figure S13. From the QY, the maximum theoritical value of LY is determined based on equation S5, where E_g^{exp} is experimental band gap, S is the electron-hole transfer efficiency, and QY is the quantum yield.

$$LY^{calc} = \left(\frac{10^3}{E_g^{exp} \cdot 2.3} \right) \cdot S \cdot QY \tag{S5}$$

Scintillation properties of Pb-based perovskites

Table S5: Summary of scintillation properties of representative perovskites (all measured at RT)

Perovskite	Light yield (photons/MeV)	Decay time (ns))	Ref.
$CsPbI_3$ nanocrystals	1,900	1.10	[20]
$CsPbBr_3$ nanocrystals	24,000	5.97	[20]
$CsPbBr_3$ single crystals	$\sim$1,200	0.39, 7.0	[21]
$CsPbBr_3$ nanosheets	$\sim$21,000	1-10	[30]
Cs_4PbI_6 singlecrystals	$\sim$5,000	0.95, 6.86	[21]
Dual-phase Cs_4PbBr_6/$CsPbBr_3$	$\sim$6,000	3	[22]
Dual-phase $CsPbBr_3$-$CsPb_2Br_5$	19,200	3.38	[23]
$CsCu_2I_3$	12.5 ± 0.5	124.88 ± 1.63	This work
$Cs_3Cu_2I_5$	16.5 ± 3.5	840.82 ± 3.65	
$Cs_3Cu_2I_4Br$	11.0 ± 1.0	684.13 ± 22.72	
$Cs_3Cu_2I_3Br_2$	5.5 ± 0.5	604.45 ± 46.15	

Geometric consideration
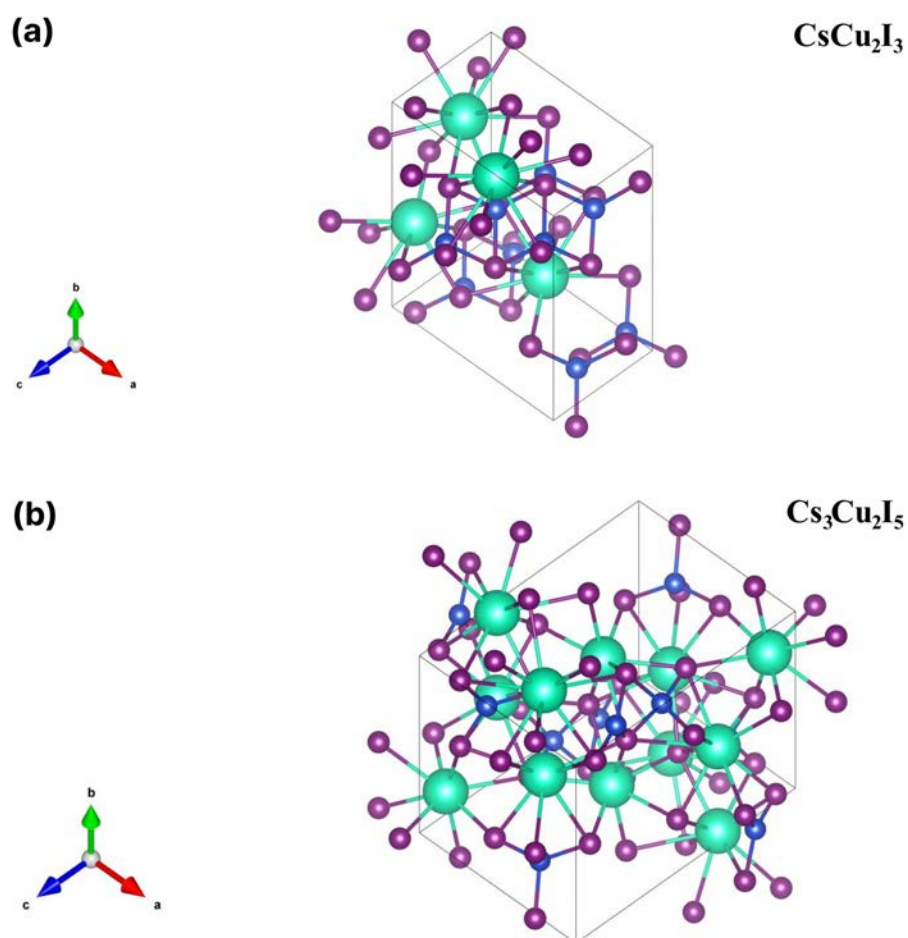
Figure S14: Visualisations of (a) 1D $CsCu_2I_3$ and (b) 0D $Cs_3Cu_2I_5$ crystal structure from structural files.[2]

Table S6: Bond length and bond angle between metal to its certain halide $CsCu_2I_3$ and $Cs_3Cu_2I_5$ CHP as obtained from CIFs.

CHP	Cu1-I1 (Å)	Cu1-I2 (Å)	I1-Cu1-I1 (deg)	I1-Cu1-I2 (deg)
$CsCu_2I_3$	2.61	2.69	116.42	108.89
$Cs_3Cu_2I_5$	2.56	2.52	117.07	121.45

References

[1] N. Doebelin and R. Kleeberg, *J. Appl. Cryst.*, 2015, **48**, 1573–1580.

[2] G. K. Grandhi, N. S. M. Viswanath, H. B. Cho, J. H. Han, S. M. Kim, S. Choi and W. B. Im, *J. Phys. Chem. Lett.*, 2020, **11**, 7723–7729.

[3] R. J. Elliott, *Phys. Rev.*, 1957, **108**, 1384–1389.

[4] J. T. Randall and M. H. F. W. Wilkins, *Proc. R. Soc. Lond. A*, 1945, **184**, 365–389.

[5] M. D. Birowosuto, D. Cortecchia, W. Drozdowski, K. Brylew, W. Lachmanski, A. Bruno and C. Soci, *Sci. Rep.*, 2016, **6**, 37254.

[6] N. Fairley, V. Fernandez, M. Richard-Plouet, C. Guillot-Deudon, J. Walton, E. Smith, D. Flahaut, M. Greiner, M. Biesinger, S. Tougaard, D. Morgan and J. Baltrusaitis, *Appl. Surf. Sci*, 2021, **5**, 100112.

[7] R. Clark, *Spectrochim. Acta*, 1965, **21**, 955–963.

[8] Z. Guo, J. Li, Y. Gao, J. Cheng, W. Zhang, R. Pan, R. Chen and T. He, *J. Mater. Chem. C*, 2020, **8**, 16923–16929.

[9] A. K. Arora, M. Rajalakshmi, T. R. Ravindran and V. Sivasubramanian, *J Raman Spectrosc.*, 2007, **38**, 604–617.

[10] F. H. Naqvi, S. B. Junaid and J.-H. Ko, *Materials*, 2023, **16**, 3986.

[11] Y. Chen, A. Mahata, A. D. Lubio, M. Cinquino, A. Coriolano, L. Skokan, Y. Jeong, L. Razzari, L. De Marco, A. Ruediger, F. De Angelis, S. Colella and E. Orgiu, *Adv. Opt. Mater.*, 2022, **10**, 2100439.

[12] J. Serrano, M. Cardona, T. M. Ritter, B. A. Weinstein, A. Rubio and C. T. Lin, *Phys. Rev. B*, 2002, **66**, 245202.

[13] S. Daliran, M. Khajeh, A. R. Oveisi, J. Albero and H. García, *ACS Appl. Mater. Interfaces*, 2022, **14**, 36515–36526.

[14] C.-X. Li, S.-B. Cho, D.-H. Kim and I.-K. Park, *Chem. Mater.*, 2022, **34**, 6921–6932.

[15] H. Liu, J. Xie, P. Liu and B. Dai, *Catalysts*, 2016, **6**, 120.

[16] Y. Lu, G. Li, S. Fu, S. Fang and L. Li, *ACS Omega*, 2021, **6**, 544–552.

[17] H. Zhang, L. Yang, H. Chen, W. Ma, R. Wang and G. Cao, *Mater. Chem. Front.*, 2022, **6**, 1647–1657.

[18] Z. Li, Z. Li, Z. Shi and X. Fang, *Adv. Funct. Mater.*, 2020, **30**, 2002634.

[19] C.-Y. Chen, Y.-I. Lin, P.-T. Lai, H.-C. Lin, G.-H. Tan, H.-W. Lin and R. D. Schaller, *Adv. Opt. Mater.*, 2022, **10**, 2200005.

[20] F. Maddalena, A. Xie, X. Y. Chin, R. Begum, M. E. Witkowski, M. Makowski, B. Mahler, W. Drozdowski, S. V. Springham, R. S. Rawat, N. Mathews, C. Dujardin, M. D. Birowosuto and C. Dang, *J. Phys. Chem. C*, 2021, **125**, 14082–14088.

[21] Y. Li, L. Chen, R. Gao, B. Liu, W. Zheng, Y. Zhu, J. Ruan, X. Ouyang and Q. Xu, *ACS Appl. Mater. Interfaces*, 2022, **14**, 1489–1495.

[22] F. Cao, D. Yu, W. Ma, X. Xu, B. Cai, Y. M. Yang, S. Liu, L. He, Y. Ke, S. Lan, K.-L. Choy and H. Zeng, *ACS Nano*, 2020, **14**, 5183–5193.

[23] V. Naresh, S. Singh, H. Soh, J. Lee and N. Lee, *Mater. Today Nano*, 2023, 100364.

[24] Z. Wang, R. Sun, N. Liu, H. Fan, X. Hu, D. Shen, Y. Zhang and H. Liu, *Nano Res.*, 2022, **15**, 2399–2404.

[25] Z. Zhang, H. Dierks, N. Lamers, C. Sun, K. Nováková, C. Hetherington, I. G. Scheblykin and J. Wallentin, *ACS Appl. Nano Mater.*, 2022, **5**, 881–889.

[26] Nanolumi, *Advanced Luminescent Materials & Integrative Solutions*, https://www.nanolumi.com/.

[27] E. Chua, *Personal communications*, 2021.

[28] X. Zhao, T. Jin, W. Gao, G. Niu, J. Zhu, B. Song, J. Luo, W. Pan, H. Wu, M. Zhang, X. He, L. Fu, Z. Li, H. Zhao and J. Tang, *Adv. Opt. Mater.*, 2021, **9**, 2101194.

[29] M. L. Ali, M. Khan, M. A. Al Asad and M. Z. Rahaman, *Heliyon*, 2023, **9**, e18816.

[30] Y. Zhang, R. Sun, X. Ou, K. Fu, Q. Chen, Y. Ding, L.-J. Xu, L. Liu, Y. Han, A. V. Malko, X. Liu, H. Yang, O. M. Bakr, H. Liu and O. F. Mohammed, *ACS Nano*, 2019, **13**, 2520–2525.